Talanta 296 (2026) 128433

Contents lists available at ScienceDirect

Talanta

journal homepage: www.elsevier.com/locate/talanta

Dual-quenching sensing system from Cu-MOFs/SOx to near-infrared electrochemiluminescence silver nanosheets for sensitive analysis of CEA

Yun Wang [a], Fengdi Li [a], Hao Yu [a], Xianpeng Liao [a], Kailong Liu [a], Lihua Hu [a,*], Hongmin Ma [a], Dan Wu [a], Qin Wei [a,b,**], Huangxian Ju [a,c]

[a] Collaborative Innovation Center for Green Chemical Manufacturing and Accurate Detection, Key Laboratory of Interfacial Reaction & Sensing Analysis in Universities of Shandong, School of Chemistry and Chemical Engineering, University of Jinan, Jinan, 250022, PR China
[b] Department of Chemistry, Sungkyunkwan University, Suwon, 16419, Republic of Korea
[c] State Key Laboratory of Analytical Chemistry for Life Science, School of Chemistry and Chemical Engineering, Nanjing University, Nanjing, 210023, PR China

ARTICLE INFO

Keywords:
NIR ECL
Ag nanosheets
Dual-quenching
CEA

ABSTRACT

In this study, a highly sensitive biosensor for the detection of carcinoembryonic antigen (CEA) was developed by integrating the excellent properties of a near-infrared electrochemiluminescence (NIR ECL) substance and a double ECL signal quencher. Silver nanosheets (Ag-Cys) exhibiting NIR electrochemiluminescence were synthesized via a simple chemical reaction using $AgNO_3$ and L-cysteine (L-Cys) as precursors. The incorporation of L-Cys not only reduces photochemical damage but also preserved the antigen-binding activity, facilitating the construction of a high-performance immunosensor. In addition, copper-based metal-organic frameworks coated with sarcosine oxidase (Cu-MOFs/SOx) was synthesized and employed as a double quencher toward Ag-Cys based on electron transfer and resonance energy transfer mechanisms. The resulting sensor exhibited high sensitivity and selectivity, with a wide linear range of 0.00005–100 ng mL^{-1} and a low detection limit of 43.65 fg mL^{-1}.

1. Introduction

Tumor biomarkers are widely utilized in clinical practice for disease screening, surveillance, and prognostic diagnosis. Currently, these markers are not only pivotal indicators of tumorigenesis but are also being investigated for their roles in modulating the immune system [1]. Carcinoembryonic antigen (CEA) is an acidic glycoprotein with human embryonic antigenic properties and is recognized as a tumor-associated antigen. Elevated serum CEA levels have been reported in patients with colorectal and other cancers compared to healthy individuals [2,3]. Consequently, the sensitive detection of CEA has garnered widespread interest, leading to the development of various analytical techniques such as enzyme-linked immunosorbent assays (ELISA) [4], electrochemical immunoassays [5], and other immunoassays techniques [6]. Among these, electrochemiluminescence (ECL) has emerged as a highly sensitive and selective approach for diagnostic applications. ECL involves applying a certain voltage to a luminescent substance, inducing light emission through a series of electrochemical reactions. It offers advantages such as precise electrochemical control and low background chemiluminescence [7]. NIR ECL combines the advantages of near-infrared spectroscopy with electrochemiluminescence, offering significant benefits such as reduced background interference and enhanced tissue penetration. Therefore, the development of efficient NIR ECL luminescent clusters is crucial for advancing bioanalytical and sensing capabilities [8,9].

Inorganic-organic hybrid materials, which incorporate both inorganic and organic components, combine the advantages of each material type while allowing for precise property tuning through structural modulation. This microscopic scale hybridization enhances material homogeneity, resulting in superior electrical and optical properties that surpass those of purely inorganic or organic polymer materials. As a result, these materials have attracted significant interest for a variety of applications [10]. Among the metal conductors, silver nanostructures are particularly notable due to their unique plasmonic, optical, and thermal properties. Silver-based nanomaterials are extensively employed in optoelectronics, flexible electronics, and sensing

* Corresponding author.
** Corresponding author. Collaborative Innovation Center for Green Chemical Manufacturing and Accurate Detection, Key Laboratory of Interfacial Reaction & Sensing Analysis in Universities of Shandong, School of Chemistry and Chemical Engineering, University of Jinan, Jinan, 250022, PR China.
E-mail addresses: hulihua1206@163.com (L. Hu), sdjndxwq@163.com (Q. Wei).

https://doi.org/10.1016/j.talanta.2025.128433
Received 27 February 2025; Received in revised form 31 May 2025; Accepted 4 June 2025

technologies [11,12]. Silver nanosheets stand out due to their high aspect ratio, large surface area, and excellent electrical conductivity, offering distinct advantages over other silver nanostructures. These properties render them highly promising for applications in sensors, catalysis, biomedicine, and antimicrobial materials [13–15]. L-cysteine (L-Cys), a low-cost, environmentally friendly thiol-containing amino acid, exhibits a strong affinity for metal ions [16]. It can self-assemble on silver nanosheets via Ag–S covalent bonding, improving both biocompatibility and stability [17].

Developing an effective quenching strategy is essential for enhancing the detection performance of sandwich sensors. Commonly employed quenching mechanisms mainly include resonance energy transfer and electron transfer. In resonance energy transfer processes, the ECL emitter serves as the energy donor, while the quencher acts as the energy acceptor. When the emission spectrum of the ECL donor overlaps significantly with the UV–Vis absorption spectrum of the quencher, energy is efficiently transferred from the donor to the acceptor, leading to noticeable signal quenching [18,19]. In contrast, electron transfer-based quenching occurs when the luminescent material from its ground state to an excited state. If the energy levels of the quenching agent and the luminescent material align appropriately, electron transfer is facilitated, resulting in significant ECL signal suppression [20]. Metal-organic frameworks (MOFs), composed of metal ions and organic ligands, possess a high specific surface area, excellent structural tunability, and superior loading capacity, making them widely applicable in sensing and catalysis fields [21,22]. The incorporation of enzymes such as sarcosine oxidase (SOx) into Cu-MOFs creates composite materials that synergistically combine enzymatic activity with framework properties, leading to enhanced sensor performance through improved biocompatibility and target recognition. These properties make Cu-MOFs/SOx a suitable candidate as a quenching material for this sensor.

In this study, novel protein-like silver-cysteine hybrid nanosheets (Ag-Cys) were synthesized by using a simple and green one-step template-free seedless aqueous chemical synthesis strategy. These luminescent nanosheets are rich in functional groups, exhibiting good dispersion and stability in water, and they possess near-infrared emission, which minimizes photochemical damage. When combined with the dual quenching capabilities of Cu-MOFs/SOx composites, this system achieves unprecedented sensitivity for CEA detection through simultaneous energy and electron transfer mechanisms.

2. Experimental

2.1. Preparation of Ag-Cys-Ab_1

Aqueous solutions of $AgNO_3$ and L-Cys were combined in a molar ratio of 1:2. The pH of the solution was then raised to 10 using 1 M NaOH. The prepared mixture was subsequently refluxed at 95 °C for 2 h. Following this, the primary marker, which comprised 10 μg mL^{-1} of CEA capture antibody, was activated using EDC and NHS at 4 °C. This activated antibody was then co-incubated with Ag-Cys(1.5 mg mL^{-1}) for 12 h, ultimately yielding the desired solution of the primary marker Ag-Cys-Ab_1, as presented in Scheme 1A.

2.2. Preparation of Cu-MOFs/SOx-Ab_2

Cu-MOFs and Cu-MOFs/SOx were synthesized based on previously

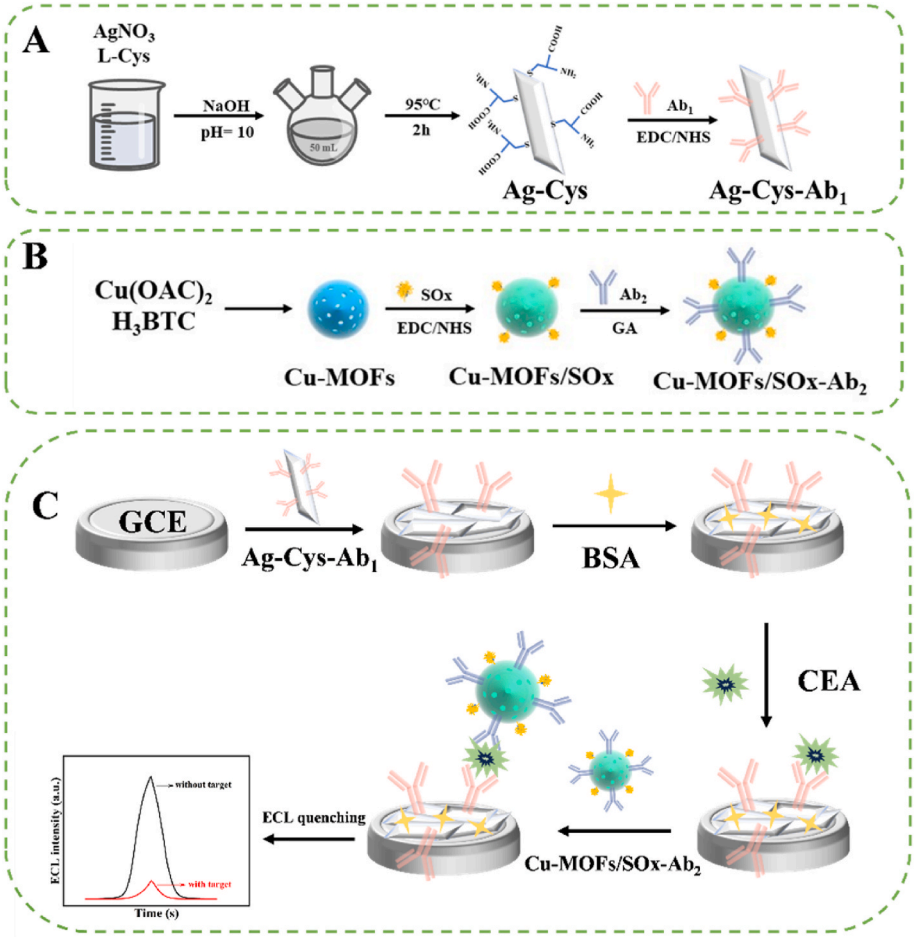

Scheme 1. (A) Preparation of Ag-Cys, (B) Preparation of Cu-MOFs/SOx, (C) Schematic diagram of the fabrication of ECL immunosensor.

reported methods [23]. To prepare solution A, 0.3 g of $Cu(CH_3COO)_2$ and 4 g of benzoic acid were dissolved in 30 mL of n-butanol, acting as modifiers. For solution B, 0.8 g of H_3BTC was dissolved in 30 mL of DMF. Solution B was slowly added to solution A with continuous stirring for 30 min. The precipitate was collected by centrifugation and washed three times with ethanol to remove any unreacted organic acids and residual solvents. Finally, the product was vacuum-dried at 60 °C for 12 h, resulting in Cu-MOFs.

To synthesize the Cu-MOFs/SOx composite, 10 mg of the prepared Cu-MOFs were suspended in 1 mL of absolute ethanol. This suspension was then combined with 6 mL of an aqueous solution containing EDC at a concentration of 0.542 mg mL^{-1} and NHS at 1.125 mg mL^{-1}. The resulting mixture was stirred vigorously for 30 min. While maintaining stirring, 3 mL of a SOx aqueous solution (0.67 mg mL^{-1}) was gradually introduced. After 4 h of continuous stirring, the Cu-MOFs/SOx composite was separated via centrifugation, washed three times with water to remove impurities, and the precipitate was collected.

Next, 100 μL of 2.5 % glutaraldehyde solution was added to 1 mL of Cu-MOFs/SOx aqueous solution (1.5 mg mL^{-1}) and gently stirred at room temperature for 2 h to allow glutaraldehyde to fully react with the amino groups on the Cu-MOFs/SOx surface. Subsequently, 100 μL of CEA capture antibody solution (10 μg mL^{-1}) was added, and the mixture was incubated at 4 °C for 12 h to enable covalent conjugation of the antibody to the Cu-MOFs/SOx surface via glutaraldehyde cross-linking. Then, 100 μL of 1 % BSA was introduced to block nonspecific binding sites. Any unbound antibodies were removed by centrifugation, and the solid product was resuspended in 1 mL of PBS (pH 7.4). This gave the sarcosine oxidase-functionalized Cu-MOFs conjugated with the carcinoembryonic antigen-recognizing antibody, forming the secondary antibody marker Cu-MOFs/SOx-Ab_2 solution, as depicted in Scheme 1B.

2.3. Fabrication of the ECL immunosensor

To construct the biosensor, a glassy carbon electrode (GCE, diameter 4 mm) was initially polished with 0.05 μm alumina powder to create a smooth surface. After rinsing the electrode with ultrapure water, 6 μL of Ag-Cys-Ab_1 was applied evenly to the polished electrode surface. After allowing the electrode to dry at 4 °C for 1 h. To block non-specific binding sites, 3 μL of BSA (0.1 wt%) was added dropwise and any excess was removed by rinsing the electrode with PBS (10 mM, pH 7.4). Next, 6 μL of CEA solutions with various concentrations were applied to the electrode surface, followed by incubation at 4 °C for 1 h to allow CEA binding. After incubation, the electrode was rinsed again with PBS to eliminate any unbound CEA. Finally, 6 μL of Cu-MOFs/SOx-Ab_2 was dropwise added to complete the biosensor construction. The resulting biosensor was stored at 4 °C until use, and ECL signals were measured in PBS solution, as depicted in Scheme 1C.

3. Results and discussion

3.1. Material characterization

The morphology and constituent elements of Ag-Cys were thoroughly investigated using scanning electron microscopy (SEM) and energy-dispersive X-ray spectroscopy (EDS). As depicted in Fig. 1A and B, Ag-Cys exhibited a lamellar structure with a relatively uniform size distribution ranging from approximately 400 to 500 nm. Fig. 1C presents the EDS image of Ag-Cys, confirming the presence of five elements: Ag, S, C, N and O. Notably, the elements S, C, N and O originated from the ligands, thereby validating the successful synthesis of the nanomaterials. The atomic percentages of Ag and S elements in the energy spectra (Fig. S1) revealed a near 1:1 ratio, indicating that silver ions were coordinated with cysteine through Ag–S bonding. This observation corroborates the successful hybridization of silver with L-Cys [24]. To

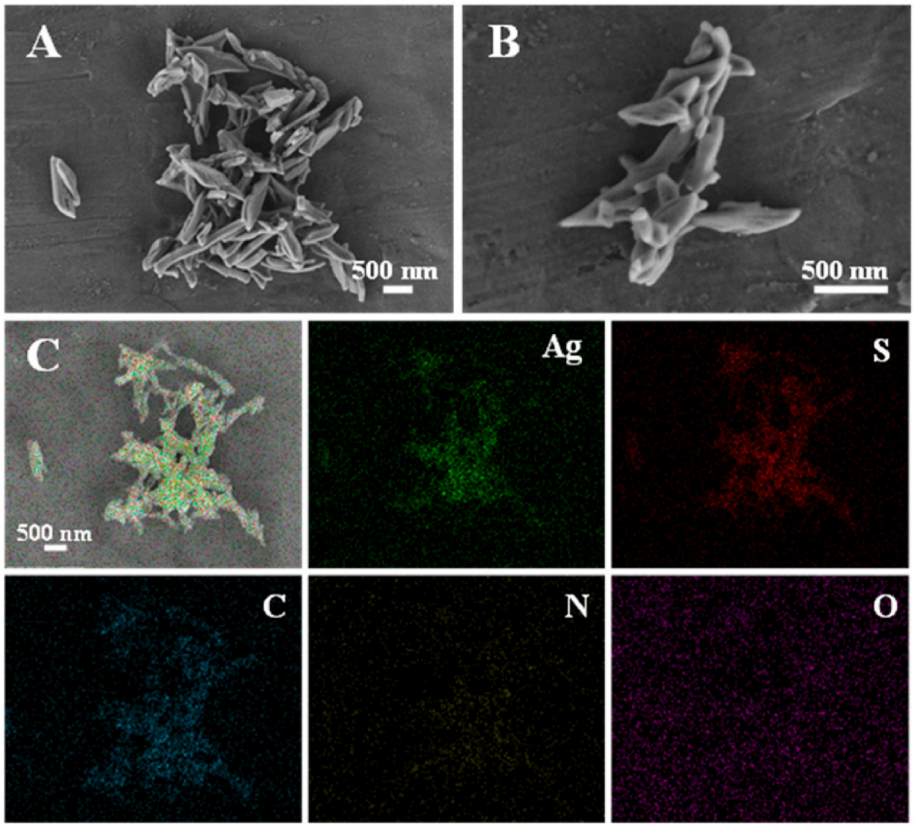

Fig. 1. (A) and (B) SEM image of Ag-Cys, (C) Mapping image of Ag-Cys.

further elucidate the physical structures and functional groups of the prepared materials, X-ray diffraction (XRD) and Fourier transform infrared spectroscopy (FTIR) were utilized. The XRD pattern (Fig. S2) revealed distinct diffraction peaks for Ag-Cys, which differed from those of the ortho-configured L-Cys. This finding indicated that the prepared Ag-Cys possessed a distinct crystal structure from its precursor, L-Cys. In essence, the nanosheets were not merely silver nanostructures coated with cysteine but rather silver nanomaterials hybridized with L-Cys [25]. FTIR spectroscopy (Fig. S3) revealed several notable features in the prepared Ag-Cys. A peak at 3440 cm^{-1} was likely attributed to the stretching vibration of the N–H bond, while a peak at 3065 cm^{-1} corresponded to the O–H stretching vibration. Clear infrared bands typical of peptides were observed, with prominent peaks at 1678 and 1631 cm^{-1}, indicating C═O stretching vibrations. Additionally, peaks at 1568 and 1488 cm^{-1} were associated with C–N stretching vibrations, while absorption bands at 1384 and 1351 cm^{-1} were attributed to CH and CH_2 groups, respectively [25,26]. These findings confirm the presence of numerous peptide bonds within Ag-Cys, providing a favorable foundation for sensor development.

X-ray photoelectron spectroscopy (XPS) was employed to investigate the elemental valence states of Ag-Cys, revealing its composition and chemical bonding. As shown in the scanning results (Fig. 2A), Ag-Cys contained elements Ag, S, C, N and O, confirming the presence of silver nanoparticles with cysteine conjugated on their surfaces. The atomic concentrations were determined as follows: C 1s-55.92 %, N 1s-10.12 %, O 1s-19.40 %, S 2p-7.29 % and Ag 3d-7.27 %. A detailed analysis of each element provided further insights. The Ag 3d spectrum (Fig. 2B) exhibited two double states, with binding energies of 368.7 and 370.5 eV for the Ag $3d_{5/2}$ component. The lower binding energy peak indicates the presence of Ag–S bonds between silver ions and cysteine, while the higher binding energy peak corresponds to metallic silver. Fig. 2C displays the S 2p spectrum, revealing asymmetric signals that suggest the existence of sulfur atoms in at least two different chemical states. The spin-orbit splitting of the S $2p_{3/2}$ binding energy at 161.2 eV corresponds to organometallic thiols covalently attached to the metal. The higher binding energy of the S $2p_{1/2}$ at 162.5 eV may be associated with the sulfur atom in the free thiol terminal group. Notably, the absence of a peak at 167.0 eV indicates that the thiol-SH groups remain unoxidized [27,28]. Fig. 2D presents the C 1s spectrum, with deconvoluted peaks corresponding to cysteine bound to the nanoparticle surface. The peak at 284.8 eV corresponds to the C–C bonds, while the peak at 286.1 eV represents the C–N and C–S bonds. The peak at 288.1 eV originates from the C═O groups within the cysteine structure [29]. These results confirm the chemical binding of cysteine to the surface of Ag nanosheets. Overall, the XPS results are in agreement with the previous characterizations, providing further confirmation of the successful synthesis and chemical structure of the Ag-Cys hybrid material.

SEM was used to examine the morphological characteristics of both Cu-MOFs and Cu-MOFs/SOx. Fig. 3A presents the SEM image of Cu-MOFs, revealing spherical particles with an approximate diameter of 100 nm. Following modification with SOx, Cu-MOFs/SOx retained a rounded morphology, as depicted in Fig. 3B, suggesting the preservation of particle integrity. To assess the successful cross-linking of Cu-MOFs and SOx, we conducted comprehensive analyses using XRD, FTIR, and

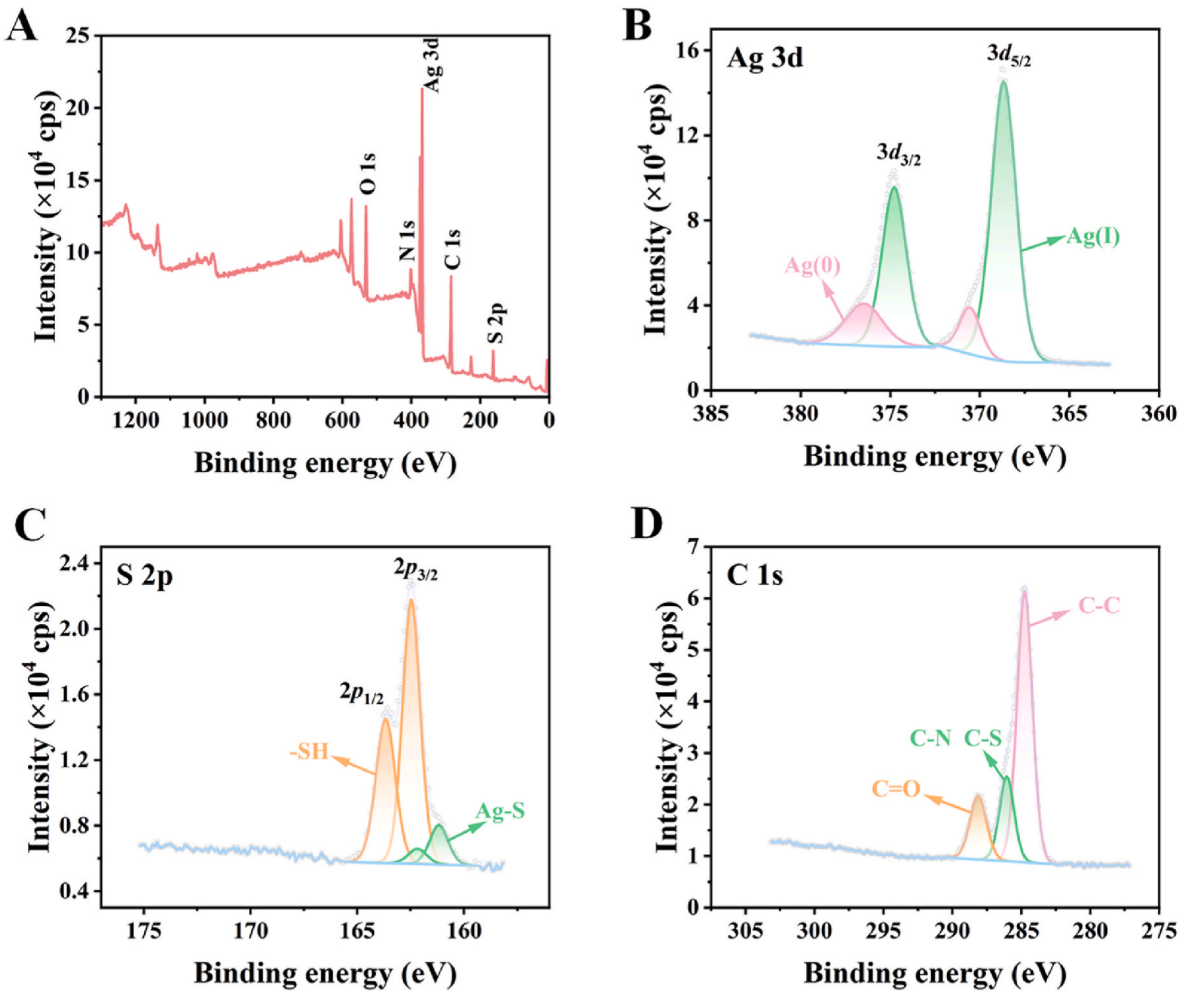

Fig. 2. XPS spectra of Ag-Cys (A) Total spectra, (B) Ag 3d, (C) S 2p, (D) C 1s.

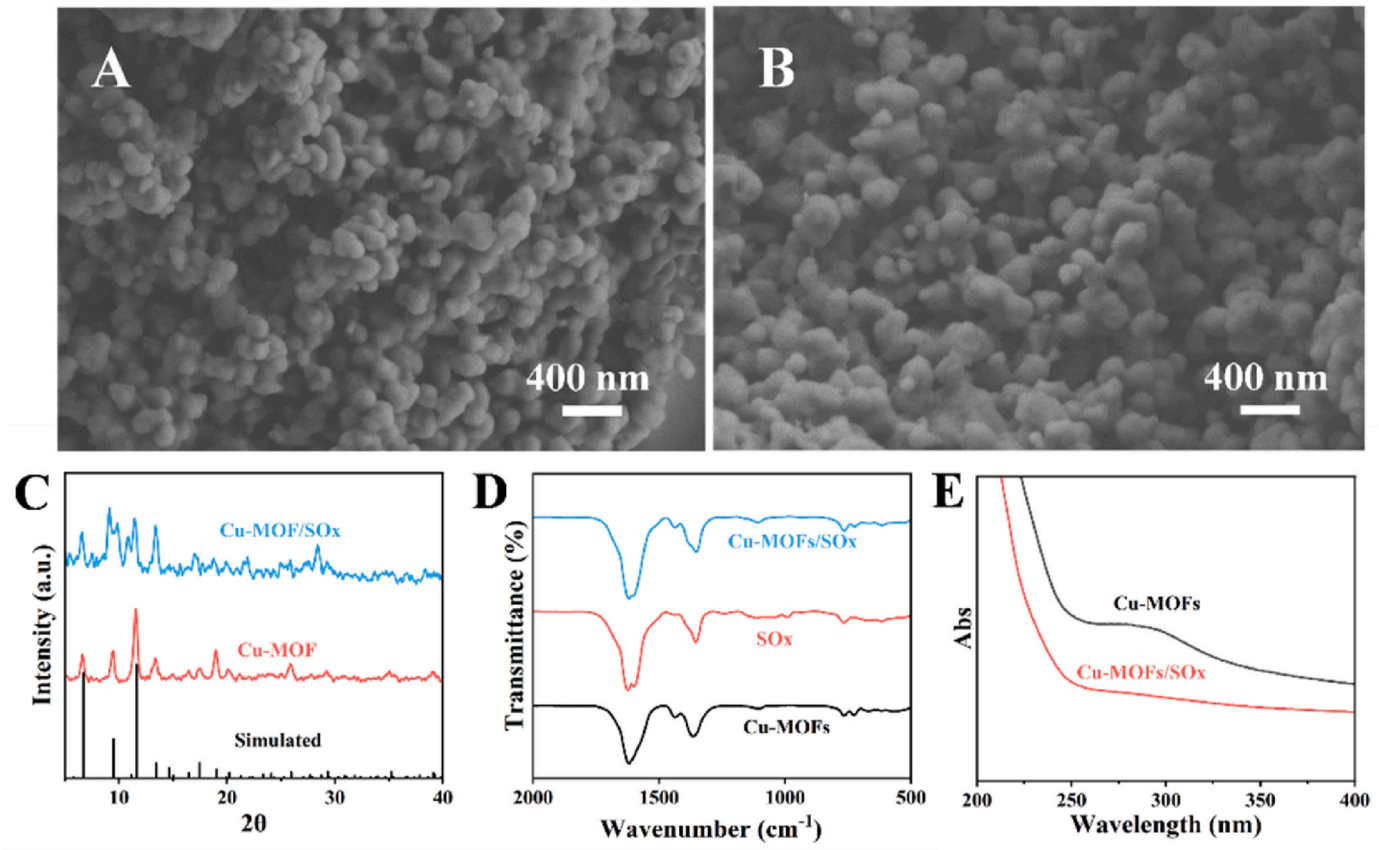

Fig. 3. SEM images of (A) Cu-MOFs, (B) Cu-MOFs/SOx, (C) XRD spectra, (D) FTIR spectra, and (E) UV–Vis absorption spectra of Cu-MOFs and Cu-MOFs/SOx.

UV–Vis absorption spectra. The XRD patterns presented in Fig. 3C indicate that the incorporation of SOx did not alter the crystal structure of Cu-MOFs. Further analysis of functional groups using FTIR spectroscopy (Fig. 3D) revealed a prominent peak at 1622 cm^{-1}, corresponding to asymmetric C═O vibration, signifying the formation of a double-tooth bridge within Cu-MOFs. Peaks observed at 1108 cm^{-1} and 1437 cm^{-1} were attributed to the C–H stretching vibration of the ligand and the C–C stretching vibration within the aromatic group, respectively. The Cu–O stretching vibration band at 726 cm^{-1} confirmed the successful coordination of oxygen ions with copper ions, thus confirming the synthesis of Cu-MOFs. When comparing the FTIR spectra of Cu-MOFs and Cu-MOFs/SOx, another distinct peak emerges at 1597 cm^{-1} in the latter. This peak is associated with the N–H planar bending vibration of the SOx-specific proteamide II moiety, providing evidence of the effective loading of SOx. UV–Vis absorption spectra (Fig. 3E) revealed that Cu-MOFs exhibit absorption peaks between 250 and 330 nm. Upon loading with SOx, these peaks disappeared, providing further evidence for the successful synthesis of Cu-MOFs/SOx [30].

3.2. Investigation of the ECL luminescence mechanism

The potential ECL mechanism of the Ag-Cys/$K_2S_2O_8$ system was explored based on the ECL luminescence behavior of Ag-Cys and related literature [31]. A comparison of the ECL and photoluminescence (PL) spectra of Ag-Cys provides insights into its surface state properties. Fig. 4A depicts the PL spectrum of Ag-Cys, peaking at 450 nm, and its

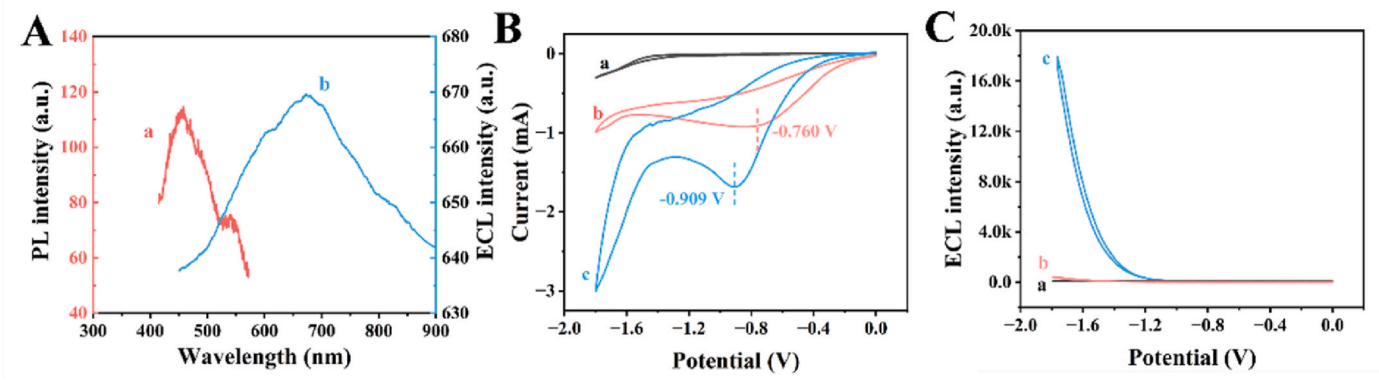

Fig. 4. (A) Fluorescence spectrum (curve a) and ECL emission spectrum (curve b) of Ag-Cys, (B) CV responses of Ag-Cys/GCE (curve a) in PBS (pH 7.4) solution and GCE (curve b) Ag-Cys/GCE (curve c) in PBS (pH 7.4, 0.1 M $K_2S_2O_8$) solution, (C) ECL response of Ag-Cys/GCE (curve a) in PBS (pH 7.4) solution and GCE (curve b), Ag-Cys/GCE (curve c) in PBS (pH 7.4, 0.1 M $K_2S_2O_8$) solution.

ECL spectrum, which shows intense emission at 675 nm. It thus appears that Ag-Cys exhibits excellent NIR emission properties, which could minimize photochemical damage, reduce background interference and facilitate detection sensitivity in complex biological environments [18,32]. In addition, the ECL spectrum is red-shifted with respect to the PL spectrum, and therefore it is inferred that the generation of Ag-Cys* is caused by the surface state jump [33,34]. From the analysis, we deduce the ECL emission mechanism of Ag-Cys to be as follows. Initially, during the scan of the electrode potential from −1.8 to 0 V, Ag-Cys underwent reduction to Ag-Cys$^{\bullet-}$ (Equation (1)). Concurrently, $S_2O_8^{2-}$ was also reduced to $SO4^{\bullet-}$ (Equation (2)). Subsequently, an oxidation reaction occurred around −1.0 V, where Ag-Cys$^{\bullet-}$ interacted preferentially with the potent oxidant $SO4^{\bullet-}$, leading to the formation of Ag-Cys* (Equation (3)). The emission of intense light followed as Ag-Cys* transited from its excited state back to the ground state, emitting photons (Equation (4)).

$$\text{Ag-Cys} + e^- \rightarrow \text{Ag-Cys}^{\bullet-} \quad (1)$$

$$S_2O_8^{2-} + e^- \rightarrow SO_4^{2-} + SO_4^{\bullet-} \quad (2)$$

$$\text{Ag-Cys}^{\bullet-} + SO_4^{\bullet-} \rightarrow \text{Ag-Cys}^* + SO_4^{2-} \quad (3)$$

$$\text{Ag-Cys}^* \rightarrow \text{Ag-Cys} + h\nu \quad (4)$$

During the potential scan from −1.8 to 0 V, the CV and ECL responses of various electrodes were evaluated. As depicted in Fig. 4B, the CV response of Ag-Cys/GCE (curve a) in PBS exhibited a weak profile, with negligible or nonexistent ECL signals. However, upon measuring in a PBS solution containing $K_2S_2O_8$, a discernible reduction peak emerged near −0.760 V for the bare electrode (curve b), attributed to the reduction of $S_2O_8^{2-}$. For the Ag-Cys-modified GCE (curve c), a reduction peak appeared around −0.909 V, accompanied by a significant increase in peak current, suggesting that Ag-Cys effectively interacts with $K_2S_2O_8$. The ECL-V curves presented in Fig. 4C further illustrate this trend. In PBS, Ag-Cys showed almost no ECL response (curve a). However, when $S_2O_8^{2-}$ was added to the PBS solution, the ECL signal intensity significantly increased, reaching approximately 18000 a.u. (curve c). The small peaks appearing on the surface of GCE in the PBS solution containing $S_2O_8^{2-}$ may be attributed to the intrinsic ECL response of $S_2O_8^{2-}$. This suggests that Ag-Cys might participate in the ECL reaction as a co-reactant luminophore. Additionally, the ECL efficiency ($Ø_{ECL}$) of the Ag-Cys/$K_2S_2O_8$ system was calculated, with the system exhibiting 1.71 times the efficiency of the standard $Ru(bpy)_3^{2+}$/$K_2S_2O_8$ system (for detailed calculation, see Supplementary Materials).

3.3. Study on double quenching mechanism of ECL

The quenching capabilities of Cu-MOFs/SOx toward Ag-Cys were investigated. As illustrated in Fig. 5A, the GCE/Ag-Cys electrode displayed an ECL signal with an intensity of approximately 17000 a.u. (curve a). However, upon modifying the GCE with Cu-MOFs/SOx (curve b), the ECL signal was significantly reduced to around 3000 a.u. These observations strongly suggest that the composite material Cu-MOFs/SOx possesses a notable quenching effect.

The band gaps of Ag-Cys and Cu-MOFs/SOx were determined using UV–Vis diffuse reflectance spectroscopy. As depicted in Fig. 5B, the band gap energy (E_g) of Ag-Cys was determined to be 4.31 eV. The flat band potential (E_{fb}) of Ag-Cys, obtained from the Mott-Schottky (M − S) plot in Fig. 5C, was calculated to be −1.20 eV. The M − S curve for Ag-Cys shows a positive slope, corresponding to an n-type semiconductor. The conduction band (CB) level was about 0.2 V lower than the E_{fb}, placing the CB at −1.40 V vs Ag/AgCl (−1.20 V vs NHE), and the valence band (VB) is computed from the bandgap of Ag-Cys of 4.31 eV according to the equation: $E_{CB} = E_{VB} - E_g$ position of 3.11 V vs NHE. In a similar manner, the E_g of Cu-MOFs/SOx was determined to be 1.81 eV (Fig. 5D). The energy levels of the highest occupied molecular orbital (HOMO) were derived from CV measurements (Fig. 5E). The E_{HOMO} is calculated to be −5.02 eV, which can be calculated to be −2.73 eV by combining with the bandgap E_{LUMO} (see Supplementary Materials for the detailed calculation procedure). Considering the Fermi energy level at −4.5 eV,

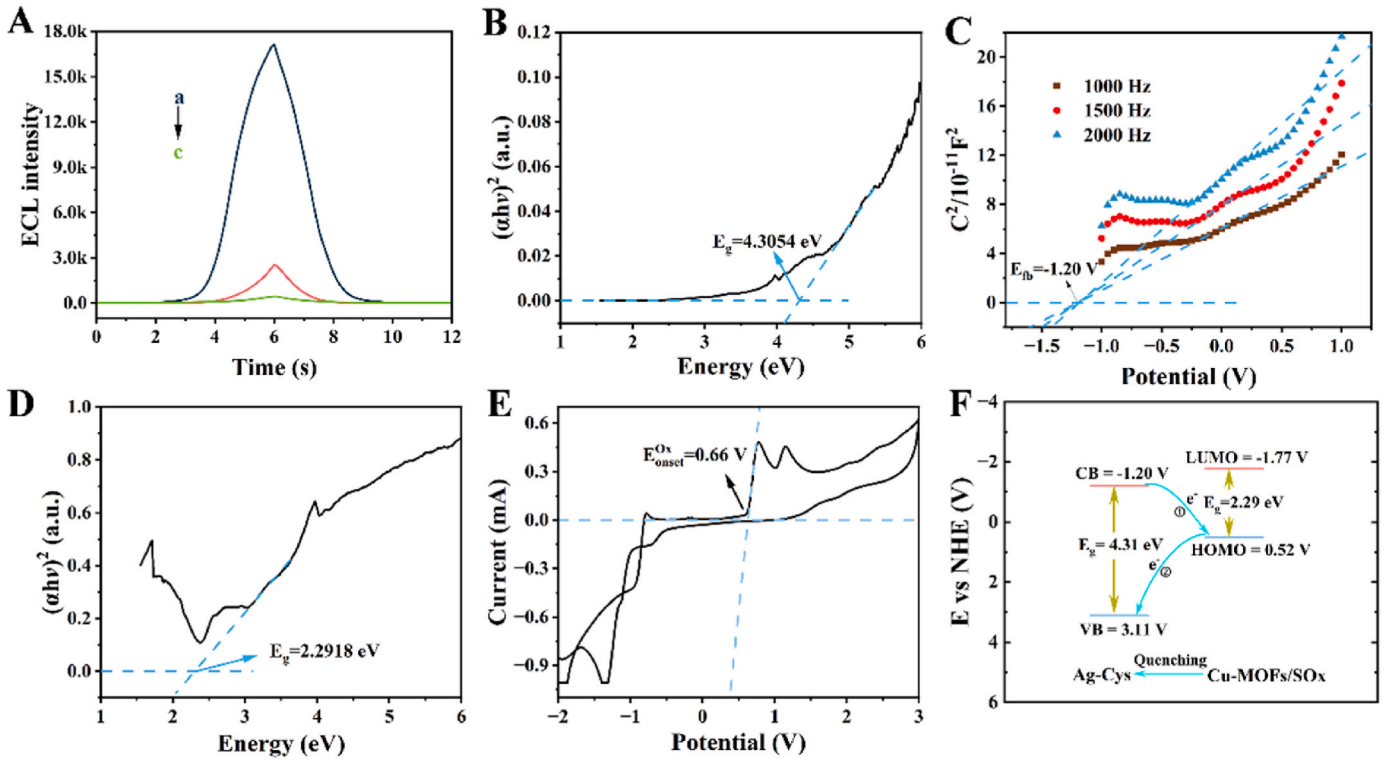

Fig. 5. (A) ECL responses of Ag-Cys/GCE (curve a), Cu-MOFs/SOx/Ag-Cys/GCE (curve b) and GCE (curve c), (B) Band gap spectrum of Ag-Cys, (C) Mott-Schottky curve of Ag-Cys, (D) Band gap spectrum of Cu-MOFs/SOx, (E) CV curve of Cu-MOFs/SOx, (F) Electron transfer mechanism.

the E_{HOMO} corresponds to 0.52 V vs. NHE, while the E_{LUMO} is approximately −1.77 V vs. NHE [35]. Reasonable energy level alignment allows electrons to transfer from Ag-Cys to Cu-MOFs/SOx, as shown in Fig. 5F. Therefore, we hypothesize: (1) During the ECL process, Ag-Cys is first electrochemically excited, and electrons transition from its VB to the CB, forming an excited state (Ag-Cys*). Since the CB level of Ag-Cys is higher than the HOMO level of Cu-MOFs/SOx, the excited state electrons will transfer from the CB of Ag-Cys to the HOMO of Cu-MOFs/SOx. This transfer process leads to the quenching of the excited state of Ag-Cys because the electrons no longer remain in the CB of Ag-Cys and cannot recombine (luminescence) radiatively back to the VB. (2) The electrons that transfer to the HOMO of Cu-MOFs/SOx will subsequently migrate to the VB of Ag-Cys since the VB level of Ag-Cys is lower than the HOMO of Cu-MOFs/SOx. This electron migration process inhibits the electrons from returning to the VB of Ag-Cys from the CB, thereby hindering electron-hole recombination and reducing the probability of radiative recombination. Since the electrons cannot recombine radiatively back to the ground state, the ECL signal is significantly quenched [36,37]. Additionally, we investigated the ECL emission spectrum of Ag-Cys alongside the UV–Vis absorption spectrum of Cu-MOFs/SOx, as depicted in Fig. S4. The ECL spectrum of Ag-Cys exhibits an emission peak in the range of 500–800 nm, which overlaps with the UV–Vis absorption range of Cu-MOFs/SOx. This overlap suggests the occurrence of resonance energy transfer (RET) between Ag-Cys and Cu-MOFs/SOx [38]. In conclusion, the ECL quenching of the sensor is primarily caused by the dual mechanisms of RET and electron transfer, which work synergistically to enhance the quenching effect [39]. To further investigate the quenching efficiency of Cu-MOFs/SOx, a series of experiments were conducted using different concentrations of Cu-MOFs/SOx for the quenching of Ag-Cys. As shown in Fig. S5, increasing the concentration of Cu-MOFs/SOx led to a decrease in the ECL signal and the relationship between Cu-MOFs/SOx concentration and quenching efficiency was analyzed using the Stern-Volmer equation ($I_0/I = 1 + k_q\tau_0[Q] = 1 + K_{SV}[Q]$), where I and I_0 denote the ECL intensities with and without Cu-MOFs/SOx, respectively, the curve was fitted to analyze the quenching kinetics [40]. The resulting K_{SV} value was found to be 3.083×10^6 g L^{-1} within the concentration range of 0–3.0 mg mL^{-1}, with a high correlation coefficient of $R^2 = 0.978$. These findings strongly suggest that Cu-MOFs/SOx exhibits a remarkable quenching effect, further supporting its potential application in related fields.

3.4. Optimization and characterization of the immunosensor construction process

The effect of the concentration of Ag-Cys, the pH of the PBS solution, the concentration of $K_2S_2O_8$, and the level of Ag-Cys quench triggered by Cu-MOFs/SOx on the sensing performance of the fabricated ECL sensor was studied. As shown in Fig. S6A, the ECL intensity reached its peak at 1.5 mg mL^{-1}, with a decrease observed when the concentration exceeded this value. This underscores that 1.5 mg mL^{-1} is the optimal concentration of Ag-Cys. The pH of the PBS solution is also vital for the sensor's effectiveness. Fig. S6B shows a steady increase in ECL intensity as the pH rises from 6.0 to 7.4, with no significant change observed beyond pH 7.4. Therefore, a pH of 7.4 was selected as optimal. The concentration of the co-reactant $K_2S_2O_8$ significantly impacts ECL performance. As shown in Fig. S6C, the intensity increases with $K_2S_2O_8$ concentration up to 100 mM, after which it starts to decrease. Therefore, 100 mM was determined as the optimal concentration for $K_2S_2O_8$. Finally, we chose the concentration of the quenching agent Cu-MOFs/SOx. Fig. S6D illustrates that the quenching efficiency increased with the concentration up to 1.5 mg mL^{-1}, after which further increases had minimal effect. Therefore, 1.5 mg mL^{-1} was selected as the optimal concentration for Cu-MOFs/SOx.

To validate the successful fabrication of the immunosensor, the CV curves associated with electrodes modified with various materials were studied. As shown in Fig. 6A, the current gradually decreased as the electrode surfaces were sequentially modified with the biomolecule antibody, BSA, antigen and secondary antibody markers, confirming the successful fabrication of the immunosensor. Further validation was obtained by investigating the relationship between ECL intensity and voltage, as depicted in Fig. 6B. The bare electrode immersed in PBS (pH 7.4) containing 100 mM $K_2S_2O_8$ exhibited a weak ECL signal (curve a). Upon modifying the GCE with Ag-Cys-Ab_1, a significant enhancement in ECL intensity was observed (curve b). Subsequently, the sequential addition of BSA (curve c) and CEA (curve d) led to a gradual decrease in ECL intensity, likely due to the interference of protein molecules in electron transport. Finally, incubation with Cu-MOFs/SOx-Ab_2 (curve e) resulted in further signal quenching, consistent with the quenching effect. These ECL and CV results provide strong evidence for the successful layer-by-layer construction of the immunosensor.

Furthermore, to elaborate on the immunosensor's construction process, electrochemical impedance spectroscopy (EIS) was employed to evaluate the performance of various modified electrodes. As depicted in Fig. 6C, the EIS outcomes for distinct modification states are presented, with the semicircle diameter serving as an indicator of electron transfer resistance (Ret). Initially, the bare electrode exhibited a small semicircle (curve a), indicating minimal Ret and free electron flow. Upon modifying the electrode with Ag-Cys-Ab_1, the semicircular area expanded (curve b), attributed to Ab_1's nonconductive nature, impeding electron transfer. Subsequent additions of BSA (curve c) and CEA (curve d) further increased the semicircular radius, confirming the successful attachment of these macromolecular proteins. Subsequently, the addition of Cu-MOFs/SOx-Ab_2 resulted in a larger semicircular arc, corroborating the immunoconjugation between the antigen and Ab_2. These results, along with simulated values from ZSimpWin software (Table S1), provide strong evidence for the successful development of the ECL immunosensor.

To evaluate the analytical capabilities of the immunosensor, CEA was utilized as the detection model across a concentration range of 0.00005–100 ng mL^{-1}. Fig. 7A displays the ECL curves, revealing a gradual variation in ECL signals with varying CEA concentrations. The corresponding calibration curve exhibited a linear regression equation of $I = 4789.76–1794.01 \lg c$ ($R^2 = 0.995$), indicating a strong correlation between the ECL signal and CEA concentration. Notably, the detection limit achieved in this study was as low as 43.65 fg mL^{-1} (Fig. 7B). This compares favorably with other CEA detection methods, exhibiting a wider detection range and a lower detection limit (Table S2). The immunosensor's high sensitivity and specificity demonstrate its potential for accurate and reliable CEA detection in practical applications.

3.5. Sensor performance

To assess the specificity of the constructed immunosensor, five clinically relevant biomarkers, such as procalcitonin (PCT), prostate-specific antigen (PSA), α-fetoprotein (AFP), immunoglobulin G (IgG) and bovine serum albumin (BSA) were selected as potential interferents. As depicted in Fig. 8A, when exposed to 10 ng mL^{-1} concentrations of these biomarkers, the ECL response exhibited minimal deviation from the control experiment, indicating a high level of specificity. Notably, the ECL intensity remained consistent both when the immunosensor was modified with 1 ng mL^{-1} CEA alone and when CEA was combined with 10 ng mL^{-1} of the aforementioned biomarkers. These observations confirm that the ECL immunosensor possesses satisfactory selectivity.

The reproducibility of the constructed biosensors was also investigated. As shown in Fig. 8B, the ECL responses from six electrodes within the same batch and from six different batches of identical electrodes were evaluated under consistent experimental conditions. The intra-batch and inter-batch RSDs were 3.61 % and 3.56 %, respectively, indicating excellent reproducibility of the sensor. Furthermore, the stability of the immunosensor was evaluated. As illustrated in Fig. 8C, the modified CEA (10 pg mL^{-1}) electrode was subjected to 10

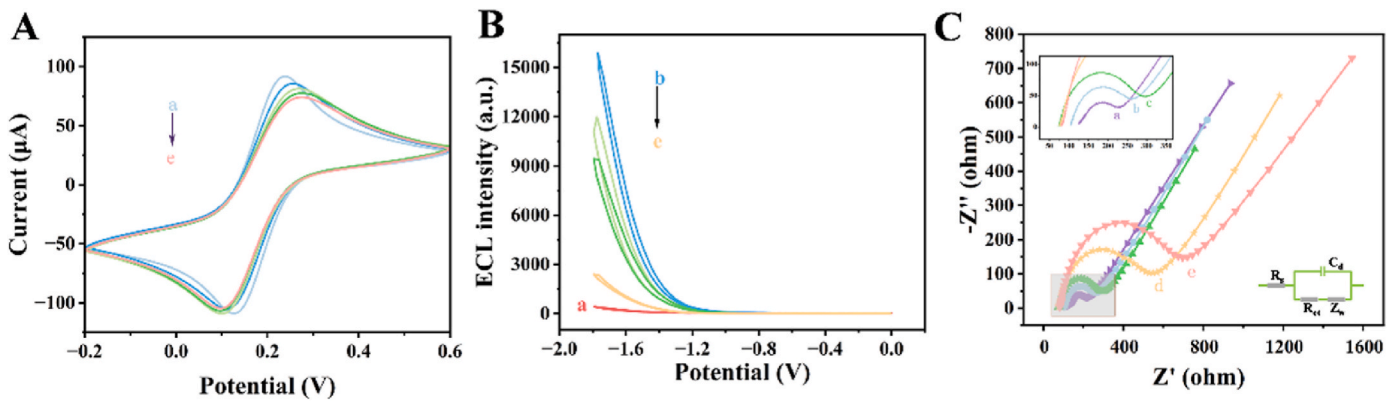

Fig. 6. GCE (a), GCE/Ag-Cys-Ab$_1$ (b), GCE/Ag-Cys-Ab$_1$/BSA (c), GCE/Ag-Cys-Ab$_1$/BSA/CEA (d), GCE/Ag-Cys-Ab$_1$/BSA/CEA/Cu-MOFs/SOx-Ab$_2$ (e) of (A) CV curves, (B) ECL-V curves and (C) EIS curves.

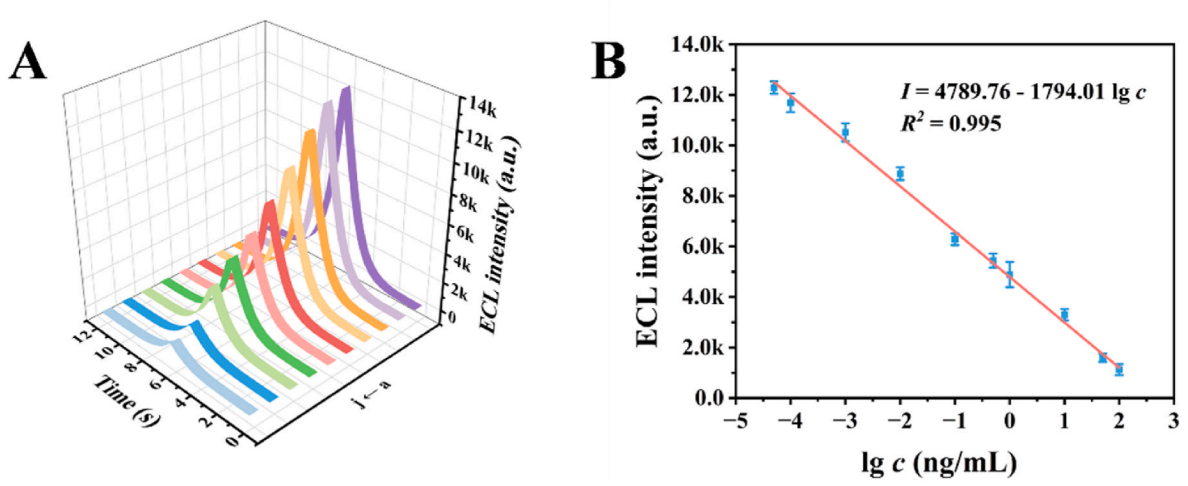

Fig. 7. (A) ECL response of the immunosensor to different concentrations of CEA from a to j: 0.00005, 0.0001, 0.001, 0.01, 0.1, 0.5, 1, 10, 50, and 100 ng mL^{-1}, (B) Calibration curves of the immunosensor to different concentrations of CEA.

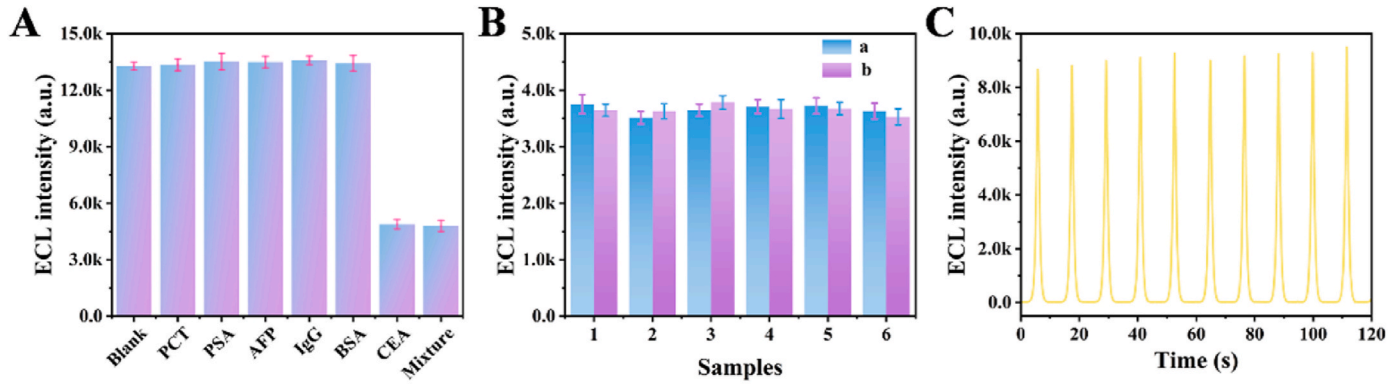

Fig. 8. (A) Immunosensor selectivity (the sensor is used to detect blanks, 10 ng mL^{-1} of PCT, PSA, AFP, IgG, BSA, and mixtures of these interfering substances with 1 ng mL^{-1} of CEA) Error bars = RSD (n = 3), (B) The reproducibility of the immunosensor detection of CEA was investigated by intra-batch (a) and inter-batch (b) analysis, (C) Stability of the ECL immunosensor over 10 cycles.

consecutive scans without significant degradation in stability. The RSD of 0.65 % validates the sensor under prolonged scanning. These results collectively demonstrate the remarkable long-term stability, reproducibility, and specificity of the immunosensor.

3.6. Sample analysis

The standard addition method was used to validate the recovery rate of the immunosensor. The human serum samples were initially diluted to 0.50 ng mL^{-1}. Various concentrations of standard CEA samples were then separately added. The results listed in Table S3 demonstrated that the immunosensor achieved recovery rates ranging from 98.88 % to

102.50 %, with an RSD of less than 4.0 %. These findings effectively established the practicality of the immunosensor for analyzing real serum samples.

4. Conclusion

In this study, an innovative ECL immunosensor was developed for CEA detection based on a dual quenching system with energy transfer and electron transfer mechanisms. Ag-Cys as an efficient ECL donor and Cu-MOFs/SOx as a quenching agent were used to establish a robust detection platform. The strong quenching effect between Ag-Cys and Cu-MOFs/SOx was verified by UV–Vis spectrum, ECL analysis and molecular orbital calculations. The prepared biosensor exhibited excellent analytical performance, achieving an ultra-low detection limit of 43.65 fg mL^{-1} and a wide linear detection range of 0.00005–100 ng mL^{-1}. In addition, the constructed sensor demonstrated excellent performance in terms of stability, reproducibility, selectivity and real sample analytical capability, providing a feasible method for efficient and highly sensitive detection of biomarkers.

CRediT authorship contribution statement

Yun Wang: Writing – original draft, Formal analysis. **Fengdi Li:** Formal analysis. **Hao Yu:** Data curation. **Xianpeng Liao:** Software. **Kailong Liu:** Validation. **Lihua Hu:** Writing – review & editing, Funding acquisition. **Hongmin Ma:** Conceptualization. **Dan Wu:** Supervision. **Qin Wei:** Resources. **Huangxian Ju:** Project administration.

Declaration of competing interest

The authors declare that they have no known competing financial interests or personal relationships that could have appeared to influence the work reported in this paper.

Acknowledgments

This study was supported by the National Natural Science Foundation of China (Nos. 21607055, 22274062), National Key Scientific Instrument and Equipment Development Project of China (No.21627809).

Appendix A. Supplementary data

Supplementary data to this article can be found online at https://doi.org/10.1016/j.talanta.2025.128433.

Data availability

No data was used for the research described in the article.

References

[1] S.K. Arya, S. Bhansali, Lung cancer and its early detection using biomarker-based biosensors, Chem. Rev. 111 (11) (2011) 6783–6809.
[2] M. Grunnet, J.B. Sorensen, Carcinoembryonic antigen (CEA) as tumor marker in lung cancer, Lung Cancer 76 (2) (2012) 138–143.
[3] M. Hasanzadeh, N. Shadjou, Y. Lin, M. de la Guardia, Nanomaterials for use in immunosensing of carcinoembryonic antigen (CEA): recent advances, TrAC, Trends Anal. Chem. 86 (2017) 185–205.
[4] P. Busson, S. Yokoyama, A. Takeuchi, S. Yamaguchi, Y. Mitani, T. Watanabe, K. Matsuda, T. Hotta, J.E. Shively, H. Yamaue, Clinical implications of carcinoembryonic antigen distribution in serum exosomal fraction—Measurement by ELISA, PLoS One 12 (8) (2017) e0183337.
[5] F.D. Martínez-Mancera, P. García-López, J.L. Hernández-López, Pre-clinical validation study of a miniaturized electrochemical immunoassay based on square wave voltammetry for early detection of carcinoembryonic antigen in human serum, Clin. Chim. Acta 444 (2015) 199–205.
[6] J. Ladd, H. Lu, A.D. Taylor, V. Goodell, M.L. Disis, S. Jiang, Direct detection of carcinoembryonic antigen autoantibodies in clinical human serum samples using a surface plasmon resonance sensor, Colloids Surf., B Biointerfaces 70 (1) (2009) 1–6.
[7] Z. Liu, W. Qi, G. Xu, Recent advances in electrochemiluminescence, Chem. Soc. Rev. 44 (10) (2015) 3117–3142.
[8] S. Diao, G. Hong, A.L. Antaris, J.L. Blackburn, K. Cheng, Z. Cheng, H. Dai, Biological imaging without autofluorescence in the second near-infrared region, Nano Res. 8 (9) (2015) 3027–3034.
[9] X. Zhu, Y. Song, X. Wang, Y. Zhou, Y. Chai, R. Yuan, Copper nanoclusters electrochemiluminescence with tunable near-infrared emission wavelength for ultrasensitive detection of matrix metalloproteinase-2, Biosens. Bioelectron. 238 (2023) 115580.
[10] S.H. Mir, L.A. Nagahara, T. Thundat, P. Mokarian-Tabari, H. Furukawa, A. Khosla, Review—Organic-inorganic hybrid functional materials: an integrated platform for applied technologies, J. Electrochem. Soc. 165 (8) (2018) B3137–B3156.
[11] A. Loiseau, V. Asila, G. Boitel-Aullen, M. Lam, M. Salmain, S. Boujday, Silver-based plasmonic nanoparticles for and their use in biosensing, Biosensors 9 (2) (2019) 78.
[12] S. Yao, Y. Zhu, Wearable multifunctional sensors using printed stretchable conductors made of silver nanowires, Nanoscale 6 (4) (2014) 2345–2352.
[13] S. Chernousova, M. Epple, Silver as antibacterial agent: ion, nanoparticle, and metal, Angew. Chem. Int. Ed. 52 (6) (2012) 1636–1653.
[14] S. Zhang, C. Liu, G. Zhang, Y. Chen, F. Shang, Q. Xia, W. Yang, Full review: the progress and developing trends of nanosheet-based sensing applications, Coord. Chem. Rev. 433 (2021) 213742.
[15] B. Mendoza-Sánchez, Y. Gogotsi, Synthesis of two-dimensional materials for capacitive energy storage, Adv. Mater. 28 (29) (2016) 6104–6135.
[16] L.B. Poole, The basics of thiols and cysteines in redox biology and chemistry, Free Radic. Biol. Med. 80 (2015) 148–157.
[17] C. Siva, C.N. Iswarya, P. Baraneedharan, M. Sivakumar, L-Cysteine assisted formation of mesh like Ag_2S and Ag_3AuS_2 nanocrystals through hydrogen bonds, Mater. Lett. 134 (2014) 56–59.
[18] M. Wei, X. Du, D. Jiang, Y. Zhang, X. Shan, W. Wang, H. Shiigi, Z. Chen, Highly efficient near-infrared electrochemiluminescence resonance energy transfer system for biosensing: nonmetallic plasmon mediated well-matched energy donor-acceptor pair, Biosens. Bioelectron. 236 (2023) 115420.
[19] J. Li, W. Lai, C. Ma, C. Zhao, P. Li, M. Jiang, M. Wang, S. Chen, C. Hong, MnO_2 nanosheet/polydopamine double-quenching $Ru(bpy)_3^{2+}$@TMU-3 electrochemiluminescence for ultrasensitive immunosensing of alpha-fetoprotein, ACS Appl. Nano Mater. 5 (10) (2022) 14697–14705.
[20] L. Luo, X. Liu, X. Bi, L. Li, T. You, Dual-quenching effects of methylene blue on the luminophore and co-reactant: application for electrochemiluminescent-electrochemical ratiometric zearalenone detection, Biosens. Bioelectron. 222 (2023) 114991.
[21] M.G. Campbell, S.F. Liu, T.M. Swager, M. Dinca, Chemiresistive sensor arrays from conductive 2D metal-organic frameworks, J. Am. Chem. Soc. 137 (43) (2015) 13780–13783.
[22] L. Jiao, Y. Wang, H.L. Jiang, Q. Xu, Metal-organic frameworks as platforms for catalytic applications, Adv. Mater. 30 (37) (2018) e1703663.
[23] C. Chen, Y.-L. Wang, X. Lin, S.-H. Ma, J.-T. Cao, Y.-M. Liu, Cu-MOFs/GOx bifunctional probe-based synergistic signal amplification strategy: toward highly sensitive closed bipolar electrochemiluminescence immunoassay, ACS Appl. Mater. Interfaces 15 (19) (2023) 22959–22966.
[24] B. Mukherjee Tarachand, M. Saxena, Y.-K. Kuo, G.S. Okram, S. Dam, S. Hussain, A. Lakhani, U. Deshpande, T. Shripathi, Ag-nanoinclusion-induced enhanced thermoelectric properties of Ag_2S, ACS Appl. Energy Mater. 2 (9) (2019) 6383–6394.
[25] W. Chen, L. Zheng, M. Wang, Y. Chi, G. Chen, Preparation of protein-like silver–cysteine hybrid nanowires and application in ultrasensitive immunoassay of cancer biomarker, Anal. Chem. 85 (20) (2013) 9655–9663.
[26] T. Huang, Q. Meng, G. Jie, Silver nanowires-based signal amplification for CdSe quantum dots electrochemiluminescence immunoassay, Biosens. Bioelectron. 66 (2015) 84–88.
[27] C. Battocchio, I. Fratoddi, L. Fontana, E. Bodo, F. Porcaro, C. Meneghini, I. Pis, S. Nappini, S. Mobilio, M.V. Russo, G. Polzonetti, Silver nanoparticles linked by a Pt-containing organometallic dithiol bridge: study of local structure and interface by XAFS and SR-XPS, Phys. Chem. Chem. Phys. 16 (23) (2014) 11719–11728.
[28] Z. Dong, X. Yang, Q. Pan, Y. Ao, J. Du, M. Zhai, L. Zhao, Performance and mechanism of selective adsorption of silver to L-cysteine functionalized cellulose microsphere, Cellulose 27 (6) (2020) 3249–3261.
[29] M. Marchioni, C. Battocchio, Y. Joly, C. Gateau, S. Nappini, I. Pis, P. Delangle, I. Michaud-Soret, A. Deniaud, G. Veronesi, Thiolate-capped silver nanoparticles: discerning direct grafting from sulfidation at the metal–ligand interface by interrogating the sulfur atom, J. Phys. Chem. C 124 (24) (2020) 13467–13478.
[30] Y.-N. Hao, C.-C. Qu, Y. Shu, J.-H. Wang, W. Chen, Construction of novel nanocomposites (Cu-MOF/GOD@HA) for chemodynamic therapy, Nanomaterials 11 (7) (2021) 1843.
[31] L. Feng, L. Wu, F. Xing, L. Hu, J. Ren, X. Qu, Novel electrochemiluminescence of silver nanoclusters fabricated on triplex DNA scaffolds for label-free detection of biothiols, Biosens. Bioelectron. 98 (2017) 378–385.
[32] J.-L. Liu, J.-Q. Zhang, Z.-L. Tang, Y. Zhuo, Y.-Q. Chai, R. Yuan, Near-infrared aggregation-induced enhanced electrochemiluminescence from tetraphenylethylene nanocrystals: a new generation of ECL emitters, Chem. Sci. 10 (16) (2019) 4497–4501.
[33] J. Liu, L. Yang, S. Li, K. Zhang, X. Zhou, G. Li, L. Wu, Y. Qin, Near-infrared electrochemiluminescence biosensors facilitated by thermally activated delayed fluorescence (TADF) emitters for ctDNA analysis, Biosens. Bioelectron. 251 (2024) 116103.

[34] Z. Ding, B.M. Quinn, S.K. Haram, L.E. Pell, B.A. Korgel, A.J. Bard, Electrochemistry and electrogenerated chemiluminescence from silicon nanocrystal quantum dots, Science 296 (5571) (2002) 1293–1297.
[35] X. Dong, G. Zhao, Y. Li, Q. Zeng, H. Ma, D. Wu, X. Ren, Q. Wei, H. Ju, Dual-mechanism quenching of electrochemiluminescence immunosensor based on a novel ECL emitter polyoxomolybdate-zirconia for 17β-Estradiol detection, Anal. Chem. 94 (37) (2022) 12742–12749.
[36] X. Dong, X. Zhang, Y. Du, J. Liu, Q. Zeng, W. Cao, Q. Wei, H. Ju, Zirconium dioxide as electrochemiluminescence emitter for D-dimer determination based on dual-quenching sensing strategy, Biosens. Bioelectron. 236 (2023) 115437.
[37] Z. Weng, Z. Li, Y. Zhang, M. Zhang, Z. Huang, W. Chen, H. Peng, Gold nanocluster probe-based electron-transfer-mediated electrochemiluminescence sensing strategy for an ultrasensitive copper ion detection, Anal. Chem. 94 (45) (2022) 15896–15901.
[38] L. Hu, T. Shi, J. Chen, Q. Cui, H. Yu, D. Wu, H. Ma, Q. Wei, H. Ju, Dual-quenching electrochemiluminescence resonance energy transfer system from CoPd nanoparticles enhanced porous g-C_3N_4 to FeMOFs-sCuO for neuron-specific enolase immunosensing, Biosens. Bioelectron. 226 (2023) 115132.
[39] X. Wang, D. Jiang, M. Dong, Y. Chen, W. Wang, Z. Sun, H. Li, H. Shiigi, Z. Chen, Dual-mechanism quenching electrochemiluminescence system by coupling energy transfer with electron transfer for sensitive competitive aptamer-based detection of furanyl fentanyl in food, J. Agric. Food Chem. 72 (40) (2024) 22360–22368.
[40] T. Shi, L. Hu, J. Chen, Q. Cui, H. Yu, Y. Li, D. Wu, H. Ma, Q. Wei, H. Ju, Dual-quenching electrochemiluminescence system based on resonance energy transfer from gold dendrite@polypyrrole core–shell nanoparticles enhanced g-C_3N_4 to ZnONFs@PDA-sCuO for procalcitonin immunosensing, Sensor. Actuator. B Chem. 371 (2022) 132591.